Magnetically Responsive Janus Nanoparticles with Catalytic Properties for the Treatment of Methyl Orange Wastewater

Yue Gao *, Dan Xue *, Hao Yan *, Xuan Qi *, Jinfeng Du , Suixin He , Wei Xia , Junfeng Zhang

Posted Date: 25 November 2025

doi: 10.20944/preprints202511.1945.v1

Keywords: magnetically responsive; janus particles; patch-like amphiphilic modification; dye wastewater treatment

 doi:10.20944/preprints202511.1945.v1

Article

Magnetically Responsive Janus Nanoparticles with Catalytic Properties for the Treatment of Methyl Orange Wastewater

Yue Gao [1,*], Dan Xue [2,*], Hao Yan [1,*], Xuan Qi [1,*], Jinfeng Du [1], Suixin He [2], Wei Xia [1] and Junfeng Zhang [3]

[1] College of Chemical and Materials Engineering, Hainan vocational University of Science and Technology, Hainan, 571126, China

[2] School of Chemical Engineering, University of Science and Technology Liaoning, Anshan 114051, China

[3] School of Chemistry and Chemical Engineering, Hainan University

* Correspondence: yueyuezcs@163.com (Y.G.); danxue@ustl.edu.cn (D.X.); yanhao0898@126.com (H.Y.); 7duan@163.com (X.Q.)

Abstract

This article presents the design, synthesis and application of novel $C_8/PW_{12}O_{40}^{3-}$–IL Janus nanopaticles for highly efficient, recyclable catalytic degradation of methyl orange (MO) in wastewater. The catalyst's innovative asymmetric architecture comprises a hydrophobic C_8 hemisphere that selectively adsorbs and pre-concentrates MO molecules, and a catalytic phosphotungstate-ionic liquid hemisphere that activates oxidants to generate hydroxyl radicals for rapid dye degradation. A magnetic Fe_3O_4 core facilitates instantaneous catalyst recovery. This "collect, degrade, and separate" mechanism synergistically results in exceptional performance, surpassing that of many conventional homogeneous and heterogeneous systems, as validated through comparative analysis. This work establishes a strategic paradigm for designing smart, multifunctional materials that combine targeted interfacial engineering with practical recyclability for advanced environmental remediation.

Keywords: magnetically responsive; Janus nanoparticles; catalytic properties; methyl orange degradation; wastewater treatment

1. Introduction

With social progress and rising industrialization, environmental pollution from industrial and agricultural production has intensified. In recent years, China's environmental protection laws and regulations have been strengthened, and pollution control technologies have advanced, effectively curbing further deterioration. At the same time, the demand for low-cost, high-efficiency, next-generation environmental technologies has become increasingly prominent.

Dyes are extensively applied in textiles, dyeing, papermaking, leather, coatings, and dye manufacturing [1]. Among them, azo dyes are the most widely used because of their low production cost and affordability.Currently, over 3,000 azo dyes are available on the market, with more than 100 commonly used in textile dyeing [2]. Statistical data show that approximately 10–15% of dyes remain unfixed on fibers during the dyeing process, leading to the generation of large volumes of dye-containing wastewater [3]. Dye wastewater is characterized by high chroma, complex composition, and low biodegradability [4]. It is biologically toxic and can cause irritation to human skin, eyes, and the respiratory system.

Currently, dye wastewater treatment methods are classified into physical [5], biological [6], and chemical [7] processes. Physical methods primarily involve adsorption and membrane separation. Adsorption is effective for low-concentration dyeing wastewater, but improper application may lead

 doi:10.20944/preprints202511.1945.v1

to secondary pollution. Membrane separation, although efficient, requires frequent membrane replacement, resulting in high costs. Biological methods depend on selecting appropriate microbial strains and are sensitive to factors such as pH, temperature, and wastewater composition. Consequently, their efficiency often fluctuates under varying environmental conditions. Chemical methods primarily involve Fenton, electrochemical, and catalytic processes. The Fenton process relies on chemical reagents, raising operational costs. Electrochemical methods consume electricity, adding further expense. Catalytic treatment introduces catalysts into wastewater to degrade pollutants; because the catalysts are reusable, this approach lowers costs while ensuring complete degradation [8].

A promising alternative is heterogeneous catalytic oxidation, which utilizes solid catalysts to activate oxidants for the degradation of dyes. Polyoxometalates (POMs), such as phosphotungstate have emerged as exceptional candidates due to their strong Brønsted acidity, high redox activity, and green character as metal-oxygen clusters[13]. While this improves recyclability, it often introduces new limitations: the supports can be inert, the catalytic efficiency was reduced, active sites can become blocked, and the materials may be lack of specificity for the complex dye molecules. Furthermore, even immobilization, the separation of catalyst powders from treated water via centrifugation or filtration remains energy-intensive, time-consuming, and impractical for large-scale operations. The introduction of Fe_3O_4 nanoparticles with magnetic responsive properties has been a significant advancement, the catalyst could be easily recovered by an external magnetic field.

The inefficient mass transfer and interaction between the solid catalyst surface and the target pollutant in the aqueous phase, especially for dyes that exhibit both hydrophilic and hydrophobic moieties, remain a critical challenge. Herein, we report a rational design and fabrication of magnetically responsive Janus nanoparticles (NPs) with amphiphilic and catalytic properties for the degradation of methyl orange wastewater.

The unique Janus architecture spatially segregates hydrophobic octyl (C_8) and hydrophilic polyoxometalate-ionic liquid ($PW_{12}O_{40}^{3-}$-IL) domain on a single microsphere, and then amphiphilic Janus NPs with catalytically properties are achieved. This structure mimics a solid-state surfactant, dramatically enhancing the capture and concentration of methyl orange molecules at the catalytic active sites via synergistic hydrophilic and hydrophobic interactions. Fe_3O_4 nanoparticles provide rapid magnetic separability, ensuring practical recovery and reuse. This work presents a new idea in the design of catalyst. Not only is it simple immobilisation, it is also multifunctional materials that actively promote interfacial processes for superior environmental remediation.

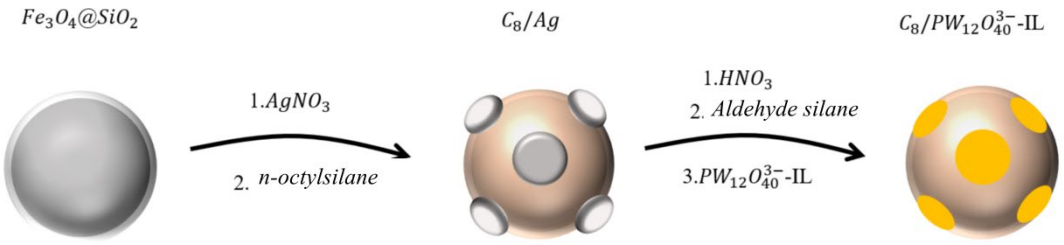

Figure 1. Schematic diagram of preparation of Janus particles with magnetic responsiveness.

2. Results and Discussion

2.1. XRD Analysis

Figure 2 presents the XRD patterns of magnetic nanoparticles. Sharp diffraction peaks appear at 2θ = 30.1º, 35.5º, 43.0º, 53.5º, 56.8º, and 62.7º, corresponding to the (220), (311), (400), (422), (511), and (440) planes of face-centered cubic Fe_3O_4 crystals (JCPDS No. 89−2355). These results confirm the successful synthesis of magnetic Fe_3O_4 NPs. The sharpness of the peaks further indicates high

 doi:10.20944/preprints202511.1945.v1

crystallinity of the Fe_3O_4 NPs [12]. According to the Bragg formula, the crystal plane size of the Fe_3O_4 NPs is 200 nm .

In the XRD pattern of Fe_3O_4@SiO_2 NPs (curve b), besides the characteristic peaks of Fe_3O_4, a broad hump appears at 2θ = 20°–30°. This is attributed to the amorphous nature of SiO_2, which does not produce sharp diffraction peaks but forms a broad diffuse band under X-ray irradiation [15]. These results confirm that a SiO_2 shell was successfully coated on the Fe_3O_4 NPs, while preserving their crystal structure [13].

For the synthesis of Fe_3O_4@SiO_2-Ag NPs, Ag^+ ions adsorbed on the Fe_3O_4@SiO_2 surface were in situ reduced to Ag nanoparticles using n-butylamine as a strong reductant. The resulting products were characterized by XRD. In curve c, new diffraction peaks at 2θ = 38.1°, 44.3°, 64.5°, and 77.5° correspond to the (111), (200), (220), and (311) planes of face-centered cubic Ag, in agreement with the standard PDF card (JCPDS No. 04-0783).

Treatment of C_8/Ag NPs with nitric acid etched away the Ag NPs, yielding "patch-structured" C_8/OH NPs. In curve d, the disappearance of Ag peaks, while the Fe_3O_4 and SiO_2 peaks remain, confirms the removal of Ag and the successful formation of C_8/OH NPs. Even after Several testing cycles, there were no changes in the XRD spectra. It meant that the nanoparticles were stable in the experiments.

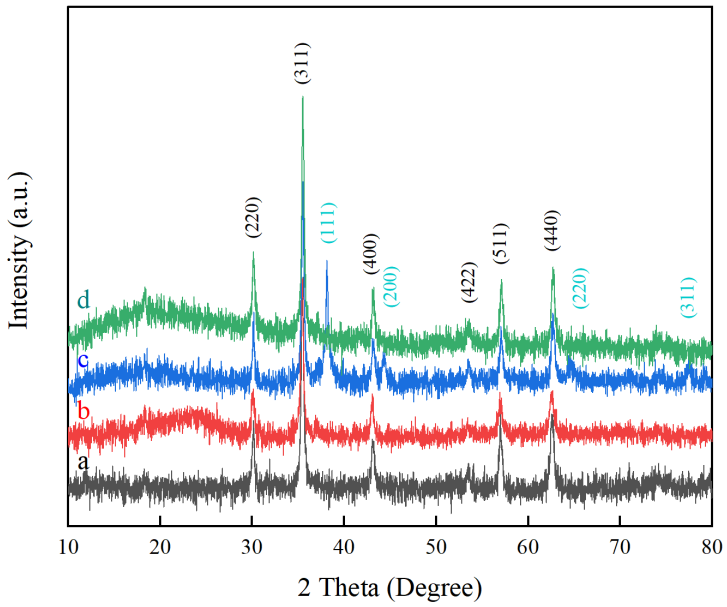

Figure 2. XRD pattern of magnetic nanoparticles. (a) Fe_3O_4 NPs; (b) Fe_3O_4@SiO_2 NPs; (c) Fe_3O_4@SiO_2-Ag NPs; (d) C_8/OH NPs.

2.2. SEM Analysis

In this study, SEM and TEM were employed to characterize the morphology of the products. Fe_3O_4 nanoparticles (NPs) are typically synthesized by chemical co-precipitation, microemulsion, thermal decomposition, hydrothermal, or solvothermal methods. Among these, the solvothermal method uses ethylene glycol as the reaction medium under high temperature and pressure, enabling the precursor to undergo redox reactions to form Fe_3O_4 NPs. Conducted in a sealed system without volatilization, this method yields products with high purity and uniform size [14]. Here, Fe_3O_4 NPs were prepared by the solvothermal method. SEM and TEM images (Figure 3a, c) reveal spherical particles with rough surfaces and uniform diameters of approximately 300 nm. In contrast, SEM and TEM images of Fe_3O_4@SiO_2 NPs (Figure 3b, d) show smooth surfaces, good dispersion without aggregation, and diameters of around 350 nm. TEM images further reveal a semi-transparent layer surrounding Fe_3O_4@SiO_2 NPs. This layer corresponds to SiO_2 generated via the sol–gel process, confirming that the Fe_3O_4 NPs were uniformly coated with a SiO_2 shell about 25 nm thick.

 doi:10.20944/preprints202511.1945.v1

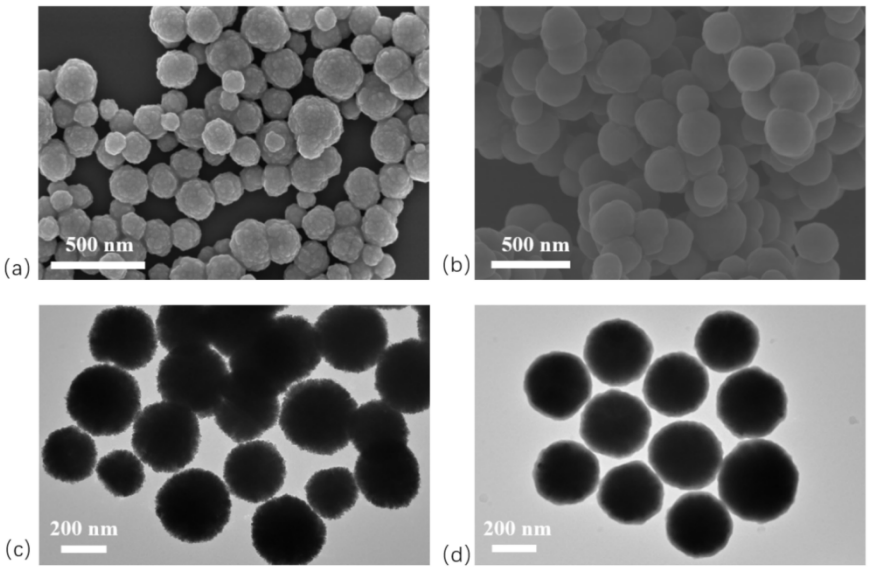

Figure 3. Electron microscope image of magnetic nanoparticles. (a) SEM image of Fe_3O_4 NPs; (b) SEM image of Fe_3O_4@SiO_2 NPs; (c) TEM image of Fe_3O_4 NPs; (d) TEM image of Fe_3O_4@SiO_2 NPs.

In this study, Ag-modified Fe_3O_4@SiO_2 nanoparticles with different particle sizes were synthesized by varying the reaction time between n-butylamine and Ag+. SEM images of SiO_2/Ag NPs (Figure 4) show that longer reaction times resulted in a greater number of Ag NPs on the Fe_3O_4@SiO_2 surface, accompanied by an increase in particle size. At a reaction time of 70 min, the Ag NPs reached an average diameter of approximately 30 nm.

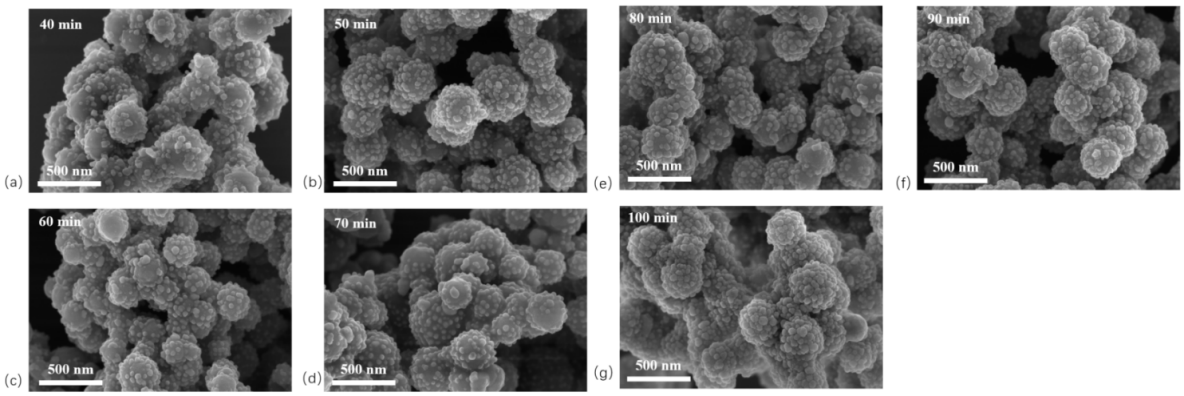

Figure 4. SEM photos of different reaction times Fe_3O_4@SiO_2-Ag NPs. (a) 40 min; (b) 50 min; (c) 60 min; (d) 70 min; (e) 80 min; (f) 90 min; (g) 100 min.

Figure 5a presents C_8/Ag NPs with smooth microsphere surfaces. Treatment with dilute nitric acid etched away the surface silver via a redox reaction, leaving pits on the microsphere surface and producing "patch-structured" C_8/OH NPs (Figure 5b). The pits exposed fresh silanol groups [15], which reacted with aldehyde silane via a sol–gel process, anchoring aldehyde silane to the pit sites and forming C_8/CHO NPs (Figure 5c). The corresponding image shows that the pits disappeared and the microspheres became smooth again. On C_8/CHO NPs, aldehyde groups reacted with the primary amine of 1-(2-aminoethyl)-3-methylimidazolium bromide via a Schiff base reaction. A subsequent ion-exchange step yielded microspheres functionalized with phosphotungstate-based ionic liquids (Figure 5d). The image shows uniform protrusions on the microsphere surface, indicating successful modification with phosphotungstate-based ionic liquids. Even after Several testing cycles, there were no changes in the morphology of the nanoparticles

 doi:10.20944/preprints202511.1945.v1

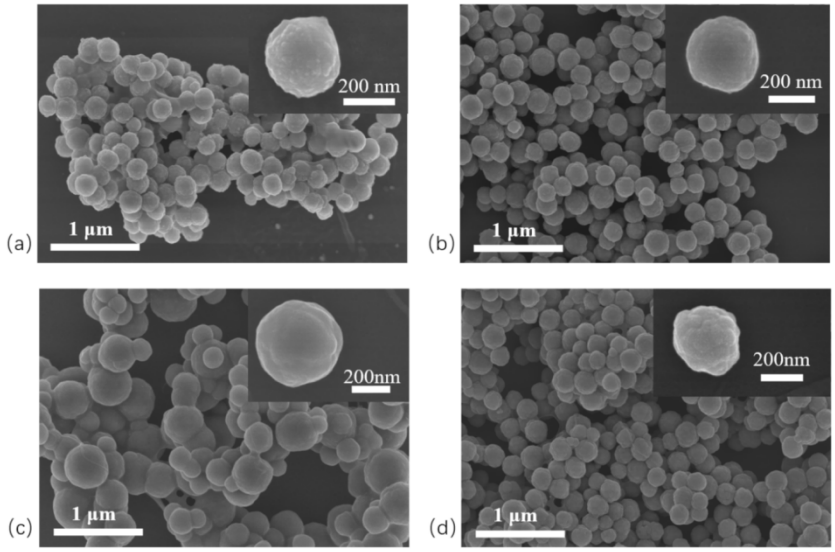

Figure 5. SEM photograph of patchy magnetic nanoparticles. (a) C_8/Ag NPs; (b) C_8/OH NPs; (c) C_8/CHO NPs; (d) $C_8/PW_{12}O_{40}^{3-}$-IL NPs.

2.3. FTIR Analysis

The chemical composition of the nanoparticles was analyzed using FTIR spectroscopy. For Fe_3O_4 NPs (Figure 6Aa), the absorption peak at 580 cm^{-1} is attributed to Fe–O bond vibrations [16]. In the spectrum of Fe_3O_4@SiO_2 microspheres (Figure 6Ab), the band at 1070 cm^{-1} corresponds to asymmetric stretching of Si–O–Si, while the band at 815 cm^{-1} is due to Si–O vibrations, confirming successful SiO_2 coating on Fe_3O_4 [12]. On Fe_3O_4@SiO_2-Ag NPs, hydroxyl groups exposed at sites without silver were reacted with octyltriethoxysilane through a sol–gel process, yielding C_8/Ag NPs. The FTIR spectrum of C_8-Fe_3O_4@SiO_2 NPs (Figure 6Ac) shows peaks at 2795 cm^{-1} and 2896 cm^{-1}, corresponding to $–CH_3$ and $–CH_2$ groups, thereby confirming successful synthesis of C_8-Fe_3O_4@SiO_2 NPs. In the spectrum of C_8/CHO NPs (Figure 6Ad), the characteristic band at 1645 cm^{-1} is assigned to –CHO stretching, confirming that aldehyde silane was successfully grafted onto C_8-Fe_3O_4@SiO_2 NPs.

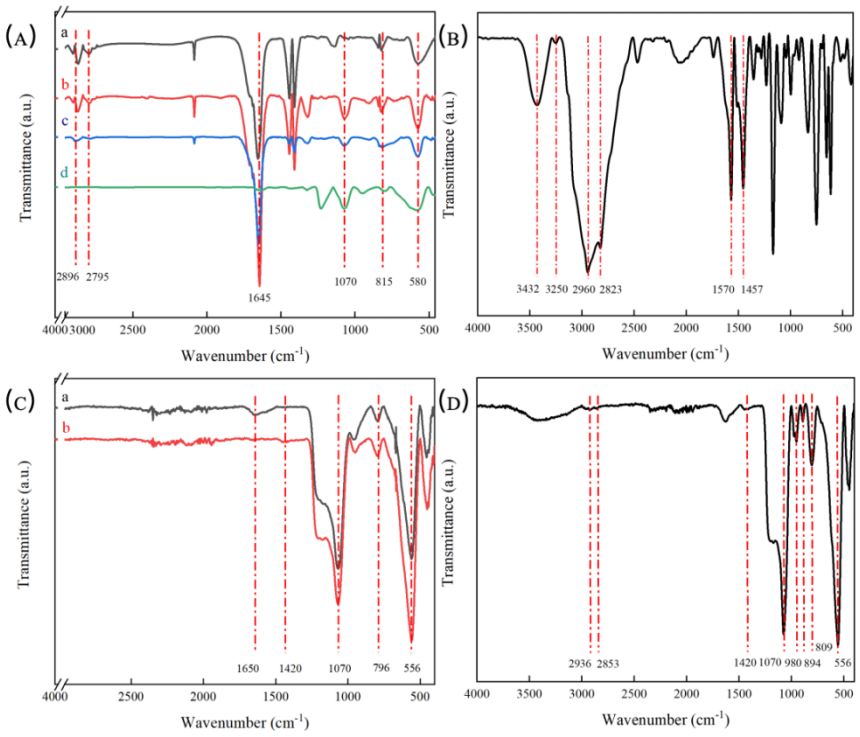

 doi:10.20944/preprints202511.1945.v1

Figure 6. (A) FTIR map of magnetic nanoparticles. (a) Fe_3O_4 NPs; (b) Fe_3O_4@SiO_2 NPs; (c) C_8/OH NPs; (d) C_8/CHO NPs, (B) FITR diagram of [2-aemin]$^+Br^-$,(C) FTIR diagram of patchy magnetic microspheres. (a) C_8/Br-IL_1 NPs; (b) C_8/Br-IL_2 NPs,(D) FTIR diagram of $C_8/PW_{12}O_{40}^{3-}$-IL NPs.

The structure of [2-aemin]$^+Br^-$ was analyzed by FTIR spectroscopy. In Figure 6B, the absorption bands at 3250 cm^{-1} and 3432 cm^{-1} confirm the presence of $–NH_2$ groups, while the bands at 1570 cm^{-1} and 1457 cm^{-1} are assigned to the imidazole ring. Additional peaks at 2960 cm^{-1} and 2823 cm^{-1} correspond to $–CH_2$ and $–CH_3$ groups, respectively. Collectively, these features confirm the successful synthesis of [2-aemin]$^+Br^-$.

Figure 6C presents the FTIR spectra of patch-like magnetic microspheres. In both curves a and b, the band at 556 cm^{-1} is attributed to Fe–O vibrations, the band at 1070 cm^{-1} to Si–O–Si asymmetric stretching, and the band at 796 cm^{-1} to Si–O vibrations, confirming the presence of Fe_3O_4@SiO_2 NPs. [2-aemin]$^+Br^-$ was grafted onto C_8/CHO NPs via a Schiff base reaction between its primary amine group and the aldehyde group of triethoxysilylbutyraldehyde, yielding C_8/Br^-–IL NPs. In curve a, the peak at 1650 cm^{-1} confirms the presence of C=N bonds, demonstrating that the $–NH_2$ group of the imidazolium salt reacted with the –CHO groups on C_8/CHO NPs, thereby forming C_8/Br^--IL_2 NPs. In curve b, the band at 1420 cm^{-1} corresponds to C–N stretching, indicating that the C=N bond was reduced to C–N by sodium borohydride, leading to the formation of C_8/Br-IL_2 NPs.

Taking advantage of the ion-exchange capability of ionic liquids, bromide ions were replaced with phosphotungstate anions in aqueous solution. FTIR spectroscopy was then used to verify the presence of phosphotungstate groups after exchange. Figure 6D presents the FTIR spectrum of $C_8/PW_{12}O_{40}^{3-}$-IL NPs obtained after ion exchange. Characteristic bands at 1070 cm^{-1} and 556 cm^{-1} correspond to Si–O–Si and Fe–O vibrations, respectively. Additional bands at 809 cm^{-1}, 894 cm^{-1}, and 980 cm^{-1} are attributed to O-b_1-W, O-b_2-W, and W=O stretching modes of phosphotungstic acid. The P–O stretching vibration also appears at 1070 cm^{-1}, overlapping with the Si-O-Si band. The band at 1420 cm^{-1} indicates the presence of C–N bonds, while absorptions at 2936 cm^{-1} and 2853 cm^{-1} correspond to $–CH_2$ and $–CH_3$ groups. Collectively, these features confirm that phosphotungstate was successfully incorporated into C_8/Br-IL_2 NPs via ion exchange, forming $C_8/PW_{12}O_{40}^{3-}$-IL NPs.

2.4. TGA Analysis

TGA analysis was conducted to investigate thermal stability and weight percent of the Janus NPs (figure 7). For the prepared solid acid catalysts, there were two weight loss areas in each curve. The first area about 100 ºC - 150 ºC was caused by the removal of absorption water in the samples. While the second area above 300 ºC was associated with C_8 group and $PW_{12}O_{40}^{3-}$-IL covered on the surface of Fe_3O_4@SiO_2 NPs, which was relative stable in thermal properties. With increased temperature, C_8 group and $PW_{12}O_{40}^{3-}$-IL were gradually decomposed to be disappeared. Furthermore, the weight percent of C_8 group and $PW_{12}O_{40}^{3-}$-IL could be calculated through TGA curves because Fe_3O_4@SiO_2 NPs could not be decomposed under 700 ºC. They were 6 % and 87 %, respectively. It meant that there was a large amount of $PW_{12}O_{40}^{3-}$-IL covered on the surface of Fe_3O_4@SiO_2 NPs.

 doi:10.20944/preprints202511.1945.v1

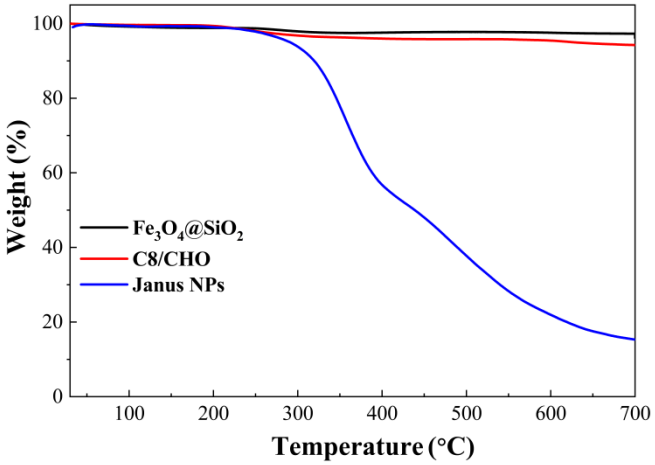

Figure 7. TGA diagram of $Fe_3O_4@SiO_2$, C_8/OH NPs, and $C_8/PW_{12}O_{40}^{3-}$-IL NPs.

2.5. XPS Analysis

To further confirm C_8 group and $PW_{12}O_{40}^{3-}$-IL had been covered on the surface of $Fe_3O_4@SiO_2$ NPs, the surface composition and chemical state of the elements were characterized by XPS. The survey spectra of Janus NPs suggested the presence of C, N, P, W and O elements (Figure 8a). Furthermore, the high solution spectra of C 1s, N 1s, and W 4f were analyzed. The peaks at 284.8, 286.2 and 288.8 eV of C 1s spectrum were ascribed to C-C, C-N and C=N bonds (Figure 8b). Meanwhile, the peaks at 400.2 and 398.3 eV of N 1s spectrum were assigned to C=N and C-N bonds (Figure 8c). It suggested that C=N group had grafted on the surface of $Fe_3O_4@SiO_2$ NPs. In addition, the characterized peaks at 36.4 eV and 38.1 eV of W 4f spectrum were signed to W 4f7/2 (WO3) and W 4f5/2 (WO3) of PW group (Figure 8d). All the spectra confirmed C_8 group and $PW_{12}O_{40}^{3-}$-IL had respectively grafted on the surface of $Fe_3O_4@SiO_2$ NPs, thus the C_8/ $PW_{12}O_{40}^{3-}$-IL NPs were achieved.

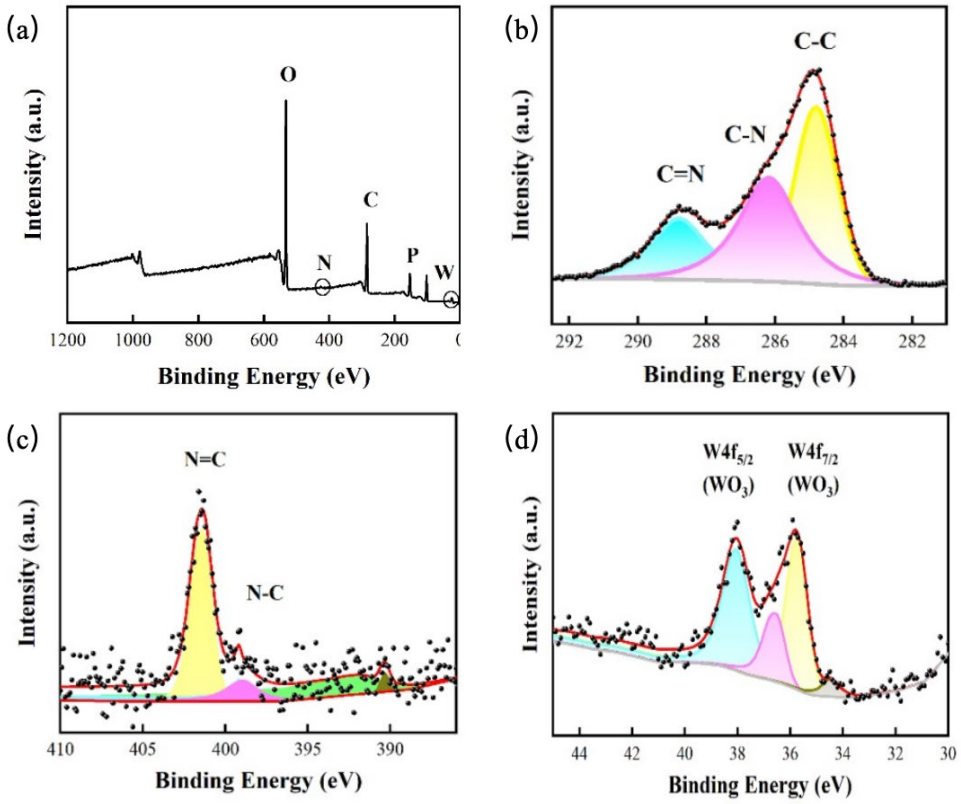

 doi:10.20944/preprints202511.1945.v1

Figure 8. XPS spectra of $C_8/PW_{12}O_{40}^{3-}$-IL Janus NPs. Survey spectrum of (a) $C_8/PW_{12}O_{40}^{3-}$-IL Janus NPs, and high solution spectra of (b) C 1s, (c) N 1s, (d) W 4f.

2.4. Emulsification Experiment

The patch-like $C_8/PW_{12}O_{40}^{3-}$-IL NPs, modified with hydrophobic C_8 and hydrophilic phosphotungstate-based ionic liquids, were employed as particle emulsifiers for immiscible oil–water systems. Here, the aqueous phase consisted of a methyl orange solution, and the oil phases included paraffin, toluene, and cyclohexane.

To evaluate the effect of oil dosage on emulsification, the volume of methyl orange solution was fixed at 30 mL and the amount of $C_8/PW_{12}O_{40}^{3-}$-IL NPs at 7.5 mg, while the paraffin dosage was varied (0.5 g, 1 g, and 2 g). The mixtures were sheared at 70 °C and 10,020 r/min for 30 min. After standing for 15 min, sedimentation of $C_8/PW_{12}O_{40}^{3-}$-IL NPs was observed in the 0.5 g and 2 g paraffin samples, indicating unstable emulsions. By contrast, the 1 g paraffin sample showed no sedimentation, with $C_8/PW_{12}O_{40}^{3-}$-IL NPs located at the water–paraffin interface (Figure 9Aa). This emulsion remained stable at room temperature for up to 15 days (Figure 9Ab, c), confirming the successful formation of a stable emulsion.

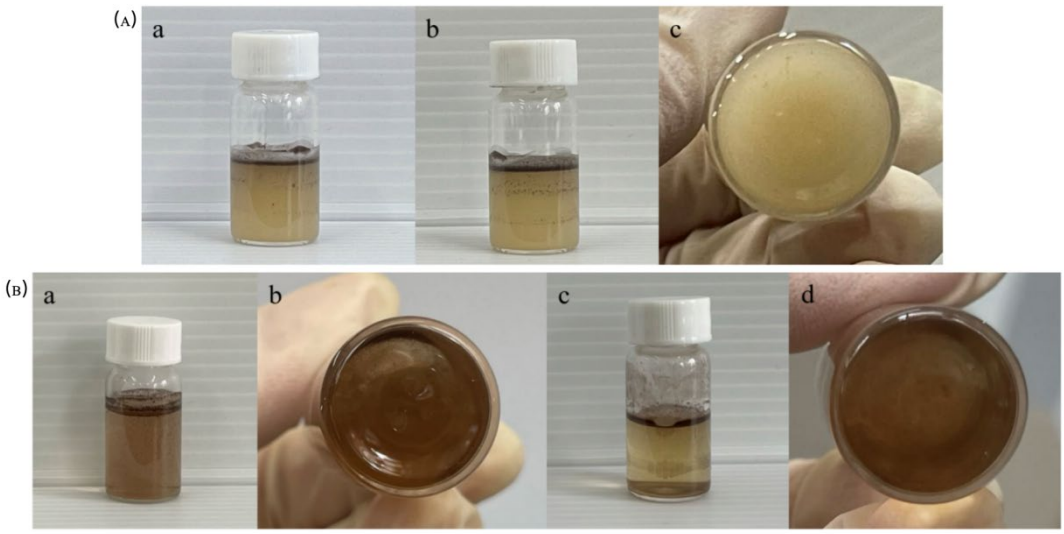

Figure 9. (A) $C_8/PW_{12}O_{40}^{3-}$-IL NPs acts as an emulsifier to emulsify aqueous and paraffin mixtures containing methyl orange. After solution shear (a) 15min, (b, c) 15 days, (B) $C_8/PW_{12}O_{40}^{3-}$-IL NPs emulsifies different oil-water mixtures. (a, b) oil phase is toluene, (c, d) oil phase is cyclohexane.

To evaluate the emulsification ability of $C_8/PW_{12}O_{40}^{3-}$-IL NPs in mixed systems with different oil and water phases, the oil phase was varied under identical conditions. Equal masses of toluene and cyclohexane were used as oil phases to emulsify aqueous methyl orange solutions, and the resulting emulsification behavior was examined. In the system with toluene as the oil phase, $C_8/PW_{12}O_{40}^{3-}$-IL NPs were clearly located at the oil–water interface (Figure 9Ba), and no sedimentation was visible from the bottom view (Figure 9Bb), indicating effective emulsification. Similarly, when cyclohexane was used as the oil phase, comparable results were observed (Figure 9Bc,d). These results demonstrate that adding 7.5 mg of $C_8/PW_{12}O_{40}^{3-}$-IL NPs as particle emulsifiers to a mixture of 30 mL methyl orange solution and 1 mL toluene yields a uniform and stable emulsion.

To examine the surface wettability of $C_8/PW_{12}O_{40}^{3-}$-IL NPs, the morphology of methyl orange/toluene emulsions stabilized by these nanoparticles was observed under an optical microscope. Optical micrographs (Figure 10) reveal that $C_8/PW_{12}O_{40}^{3-}$-IL NPs function as particle emulsifiers, stabilizing methyl orange/toluene mixtures into water-in-oil emulsions with droplet diameters of approximately 5 μm. These results confirm the amphiphilic nature of $C_8/PW_{12}O_{40}^{3-}$-IL NPs.

 doi:10.20944/preprints202511.1945.v1

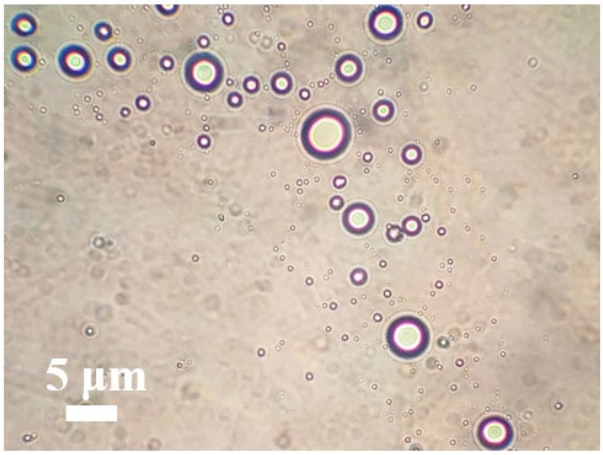

Figure 10. Optical image of $C_8/PW_{12}O_{40}^{3-}$-IL NPs emulsion containing methyl orange/toluene mixture.

2.5. Contact Angle Test

The wettability of the $C_8/PW_{12}O_{40}^{3-}$-IL NP surface was evaluated by contact angle measurements. The measured contact angle was θ = 36.404° (Figure 11), indicating that the surface is hydrophilic. This hydrophilicity is attributed to the larger surface area covered by hydrophilic groups compared with hydrophobic on $C_8/PW_{12}O_{40}^{3-}$-IL NPs. The contact angle results are consistent with the FTIR spectra, in which the absorption peaks of $–CH_2$ and $–CH_3$ appeared relatively weak.

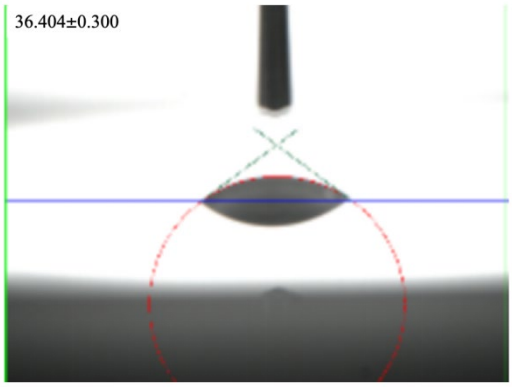

Figure 11. $C_8/PW_{12}O_{40}^{3-}$-IL NPs contact angle test.

2.6. Methyl Orange Degradation Experiment

The synthesized $C_8/PW_{12}O_{40}^{3-}$-IL NPs exhibit amphiphilicity, enabling them to function as particle emulsifiers in the methyl orange–toluene system (Figure 12). Furthermore, the phosphotungstic acid groups on their surface impart catalytic activity, allowing these NPs to act as catalysts for methyl orange degradation. In 2000, Catherine Galindo [17] reported that certain degradation products of methyl orange are aromatic compounds with oil solubility. Based on this, $C_8/PW_{12}O_{40}^{3-}$-IL NPs were employed in the methyl orange–toluene system to catalyze its degradation. Because the degradation products of methyl orange are oil-soluble, they preferentially migrate into the organic phase. This decreases their concentration in the aqueous phase, driving the forward reaction and thus facilitating more efficient degradation of methyl orange.

 doi:10.20944/preprints202511.1945.v1

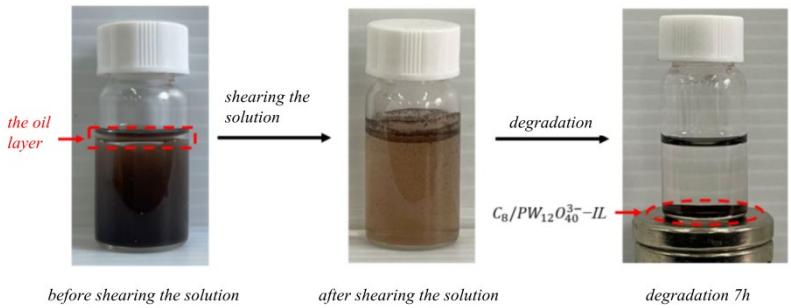

Figure 12. Image of $C_8/PW_{12}O_{40}^{3-}$-IL NPs catalyzed the degradation of methyl orange.

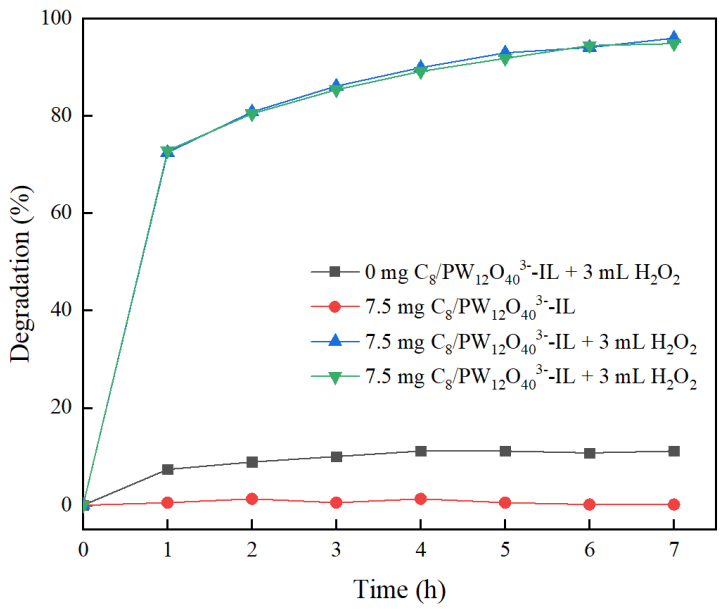

Figure 13. $C_8/PW_{12}O_{40}^{3-}$-IL NPs catalyzed the degradation of methyl orange.

The results indicate that in a 30 mL methyl orange–1 mL toluene system, the addition of 3 mL H_2O_2 followed by 7 h of magnetic stirring achieved only 11% degradation. When $C_8/PW_{12}O_{40}^{3-}$-IL NPs were used as particle emulsifiers to form a stable emulsion under identical conditions, no degradation was observed. However, upon introducing 3 mL H_2O_2 into the emulsion system, efficient degradation occurred, reaching 95.98% after 7 h (Blue line in Figure 13). This enhanced degradation arises because H_2O_2 activates $PW_{12}O_{40}^{3-}$ to form peroxo species (e.g., $\{PO_3(OH)[WO(O_2)_2]_2\}^{2-}$) with greater oxidative power than H_2O_2 itself, thereby accelerating methyl orange degradation. Increasing the H_2O_2 dosage beyond this level did not further improve degradation, as the phosphotungstate groups were already fully activated [11].

$C_8/PW_{12}O_{40}^{3-}$-IL NPs were magnetically recovered from the reaction system, washed, and reused in subsequent degradation experiments. As illustrated in the figure, the degradation efficiency showed only a slight decline with successive cycles, maintaining above 90% even after five reuses (Green line in Figure 13).

 doi:10.20944/preprints202511.1945.v1

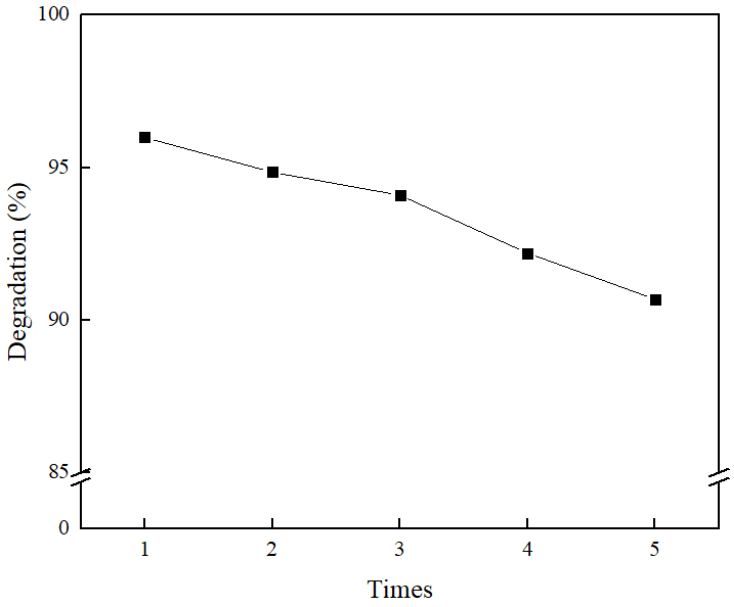

Figure 14. Catalytic activity of $C_8/PW_{12}O_{40}^{3-}$-IL NPs.

The Janus $C_8/PW_{12}O_{40}^{3-}$–IL NPs achieved efficient methyl orange (MO) degradation through a synergistic, multi-stage mechanism engineered by their asymmetric structure (in Figure 14). The hydrophobic C_8 hemisphere first acts as a concentrator, adsorbing and pre-concentrating MO molecules from the aqueous solution via hydrophobic interactions. Subsequently, the catalytic $PW_{12}O_{40}^{3-}$–IL hemisphere activates oxidants, such as H_2O_2, to generate highly reactive hydroxyl radicals (·OH), which immediately and non-selectively attack the pre-concentrated MO, primarily cleaving the azo bond (–N=N–) for decolorization and further mineralizing the aromatic fragments. Finally, the magnetic Fe_3O_4 core enables the facile separation and recovery of the entire microsphere post-reaction via an external magnetic field, completing an integrated "collect, degrade, and separate" cycle that enhances both catalytic kinetics and recyclability by preventing functional interference between the distinct hydrophobic and catalytic sites. The above catalytic mechanism is as follows.

$PW_{12}O_{40}^{3-}$ (W^{6+}) + H_2O_2 → $PW_{12}O_{40}^{5-}$ (W^{5+}) + ·OH + OH^-

$PW_{12}O_{40}^{5-}$ (W^{5+}) + H_2O_2 → $PW_{12}O_{40}^{3-}$ (W^{6+}) + ·OH + H_2O

2 H_2O_2 → ·OH + H_2O

·OH + MO → CO_2+ H_2O

Compare Janus $C_8/PW_{12}O_{40}^{3-}$–IL NPs with those of several previously published studies on the catalytic removal of methyl orange, Janus $C_8/PW_{12}O_{40}^{3-}$–IL NPs had exhibited superior catalytic properties.

Table 1. Comparison of Catalytic Properties of Janus $C_8/PW_{12}O_{43}^{-}$IL NPs with Various Photocatalysts for Methyl Orange Degradation.

Catalyst System	Catalytic Type	Optimal Conditions	Performance
This work	Visible Light Photocatalysis	60 min, 20 mg/L MO, 300 W Xe lamp	96% Degradation

 doi:10.20944/preprints202511.1945.v1

Catalyst System	Catalytic Type	Optimal Conditions	Performance
BiOClBrI	Visible Light Photocatalysis	180 min, 15 mg/L MO, 300 W Xe lamp	98% Degradation
TiO_2	UV Light Photocatalysis	Not fully specified, partial reflux	10% Degradation per reaction cycle
Porous ZnO Microflowers	Photocatalysis	300 min, 10 ppm MO, 150 mg catalyst, pH 7	Highest degradation in 300 min
UV/TiO_2 System	UV Light Photocatalysis	150 min treatment	74.12% COD Removal, 96.79% Decolorization (120 min)

3. Experiment

3.1. Materials and Methods

The chemical reagents used in this study are of analytical grade, and no additional purification was performed. The specific reagents and their sources are as follows: Ferric chloride hexahydrate, sodium acetate trihydrate, ethylene glycol, hydrochloric acid, ethanol, aqueous ammonia, tetraethyl orthosilicate (TEOS), silver nitrate, n-butylamine, octyltriethoxysilane, nitric acid, triethoxysilylbutyraldehyde, and 1-methylimidazole, provided by Sigma-Aldrich (St. Louis, MO, USA). Other reagents, including high-purity nitrogen were supplied by standard chemical suppliers

Main instruments: X-ray diffractometer (XRD), Rigaku D/MAX-2500 (Rigaku Corporation, Tokyo, Japan), used for characterizing the crystal structure of nano-ZnO. Transmission electron microscope (TEM), JEOL JEM-2100 (JEOL Ltd., Tokyo, Japan), was used to observe the sample's morphology and particle size. X-ray photoelectron spectroscopy (XPS), PHI 5000 (Physical Electronics, Chanhassen, MN, USA), was used to analyze the sample's surface chemical state. Thermogravimetric analyzer (TGA), Shimadzu DTG-60 (Shimadzu Corporation, Kyoto, Japan).

3.2. Sample Preparation

Preparation of C_8/Ag NPs

The synthesis of Fe_3O_4 and Fe_3O_4@SiO_2 nanoparticles followed our group's previous protocol [18]. It aims to create a robust, chemically inert, and uniform platform that allows for subsequent surface-specific modifications, which is a prerequisite for forming the Janus structure. In brief, 3.76 g of ferric chloride hexahydrate, 10.03 g of sodium acetate trihydrate, and 139 mL of ethylene glycol

 doi:10.20944/preprints202511.1945.v1

were placed in a 250 mL three-neck round-bottom flask and ultrasonicated for 5 min to yield a khaki solution. The mixture was transferred to a high-pressure autoclave and reacted at 200℃ for 10 h. The resulting black magnetic solids were collected using an external magnetic field, washed three times with deionized water and absolute ethanol, and freeze-dried to yield Fe_3O_4 NPs.

A total of 0.3 g Fe_3O_4 NPs and 60 mL of 0.1 M hydrochloric acid were placed in a 100 mL round-bottom flask and ultrasonicated for 2 min. The particles were collected magnetically and washed three times with deionized water. They were then dispersed in a mixture of 180 mL ethanol, 45 mL deionized water, and 3.6 mL ammonia, followed by 60 min of ultrasonication. Next, 300 μL of tetraethyl orthosilicate was added, and the suspension was stirred for 12 h. After completion, the product was magnetically recovered, washed with deionized water to neutrality, and freeze-dried to obtain brown Fe_3O_4@SiO_2 NPs.

300 mg Fe_3O_4@SiO_2 NPs, 240 mg silver nitrate, and 100 mL absolute ethanol were combined in a 150 mL round-bottom flask and ultrasonicated until dissolved. Since n-butylamine has strong reducing property, which could in-situ reduce silver ions to silver particles on the surface of Fe_3O_4@SiO_2 NPs. Subsequently, 80 μL n-butylamine was added, and the mixture was stirred at 50 °C for 70 min. The resulting product was magnetically separated, washed three times with absolute ethanol, and freeze-dried to yield Fe_3O_4@SiO_2-Ag NPs.

300 mg Fe_3O_4@SiO_2-Ag NPs and 100 mL absolute ethanol were placed in a 150 mL round-bottom flask and ultrasonicated for 1 h. Then, 6 μL octyltriethoxysilane was added, and the suspension was stirred at room temperature for 12 h. Afterward, the product was washed alternately with deionized water and ethanol, and freeze-dried to yield C_8/Ag NPs.

Octyl/hydroxyl nanoparticles (C_8/OH NPs) were synthesized by modifying our group's earlier method. In detail, 150 mg C_8/Ag NPs and 100 mL of 2 M nitric acid, which could etch the Ag NPs, were added to a 150 mL round-bottom flask and ultrasonicated for 2 h. The product was then washed alternately with deionized water and ethanol, and freeze-dried to yield C_8/OH NPs.

Octyl/aldehyde nanoparticles (C_8/CHO NPs) were prepared by optimizing our group's earlier method(in Figure 15). Briefly, 150 mg C_8/OH NPs and 100 mL absolute ethanol were placed in a 150 mL round-bottom flask and ultrasonicated for 1 h. Subsequently, 5 μL triethoxysilylbutyraldehyde was added, and the suspension was stirred at room temperature for 12 h. The resulting product was washed alternately with deionized water and ethanol, and freeze-dried to yield C_8/CHO NPs. The final yield was 78.2% based on the mass of the etched intermediates from step 3.2.2, confirming the high efficiency of the sequential grafting process.

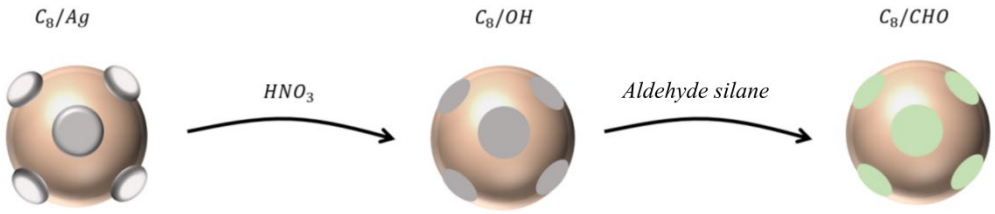

Figure 15. Schematic diagram of preparation of C_8/CHO NPs.

Preparation of 1-(2-aminoethyl)-3-Methylimidazolium Bromide

A 50 mL three-neck round-bottom flask was charged with 2.05 g 1-methylimidazole, 5.125 g 2-bromoethylamine hydrobromide, and 30 mL acetonitrile. The mixture was stirred at 80 °C until completely dissolved and then maintained at this temperature with stirring for 4 h. After cooling to room temperature, 1 g solid NaOH was added, and the suspension was stirred for 1 h, producing a white NaBr precipitate, a pale-yellow viscous product identified as 1-(2-aminoethyl)-3-methylimidazolium bromide ([(2-aemin)$^+$Br$^-$] ionic liquid), and the upper acetonitrile phase. The mixture was allowed to stand for 2 h to achieve clear phase separation. The upper acetonitrile layer

 doi:10.20944/preprints202511.1945.v1

was removed, and the lower phase was dispersed in absolute ethanol. The suspension was filtered three times to eliminate NaBr precipitates. The filtrate was then concentrated by rotary evaporation to remove ethanol, affording the ionic liquid 1-(2-aminoethyl)-3-methylimidazolium bromide ([(2-aemin)$^+$Br$^-$]) [19].

A mixture of 10 mg [(2-aemin)$^+$Br$^-$] and 10 mg C_8/CHO NPs was dispersed in 10 mL deionized water and stirred at room temperature for 6 h to form C_8/Br$^-$–IL$_1$ NPs. Sodium borohydride was then added, and the reaction was allowed to proceed under stirring for 12 h. The products were magnetically separated, washed three times with absolute ethanol and deionized water, and dried to obtain octyl/imidazolium bromide nanoparticles (C_8/Br$^-$–IL$_2$ NPs).

10 mg C_8/Br$^-$–IL$_2$ NPs and 10 mg phosphotungstic acid were dissolved in 10 mL deionized water and stirred at room temperature for 1 h. The products were then magnetically separated, washed with absolute ethanol and deionized water, and dried to yield octyl/phosphotungstate ionic liquid nanoparticles (C_8/$PW_{12}O_{40}^{3-}$-IL NPs)(in Figure 16).

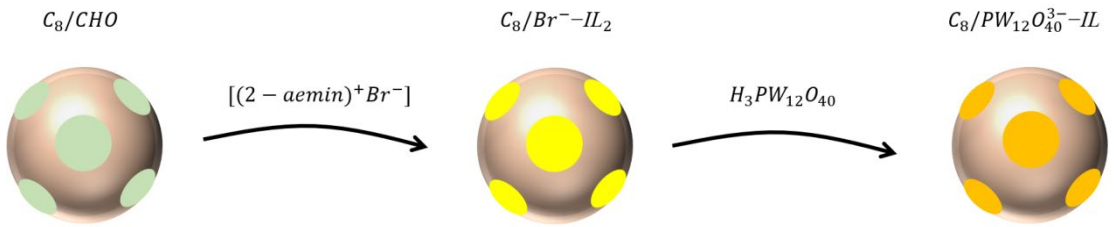

Figure 16. Schematic diagram of preparation of C_8/$PW_{12}O_{40}^{3-}$-IL NPs.

3.3. Test of Methyl Orange Wastewater

C_8/$PW_{12}O_{40}^{3-}$-IL Janus NPs C_8/$PW_{12}O_{40}^{3-}$-IL was first ultrasonicated in 30 mL of 5 mg/L methyl orange solution. Toluene was then added, and the mixture was sheared at room temperature for 30 min to form a stable water-in-oil emulsion. Hydrogen peroxide was subsequently introduced, and the suspension was stirred continuously. Aliquots were withdrawn at regular intervals to measure absorbance.

To assess the reusability of C_8/$PW_{12}O_{40}^{3-}$-IL, the nanoparticles were magnetically recovered from the degradation system. The samples were thoroughly washed with N,N-dimethylformamide and deionized water, dried, and stored for subsequent use. Their performance in treating methyl orange wastewater was re-examined under the same experimental conditions.

3.4. Material Characterization

X-ray powder diffraction (XRD) [20] was used to analyze the diffraction patterns of the materials, providing information on their chemical composition and internal atomic or molecular structure. Characteristic functional groups were identified using Fourier-transform infrared spectroscopy (FTIR) [21–23]. Material morphology was examined by field-emission scanning electron microscopy (FE-SEM) and transmission electron microscopy (TEM) [24–26]. Thermogravimetric analysis (TGA) was employed to assess the thermal stability of the materials and to determine the mass fractions of inorganic (SiO_2) and organic components (PNIPMA and PIL) [27–30].

4. Conclusions

In this study, patch-like amphiphilic C_8/$PW_{12}O_{40}^{3-}$-IL were synthesized using magnetically responsive Fe_3O_4@SiO_2 NPs as the core, functionalized with hydrophilic $PW_{12}O_{40}^{3-}$-IL and hydrophobic n-octyl . The nanoparticles acted as particle emulsifiers to stabilize methyl orange–toluene emulsions, and owing to the catalytic activity of $PW_{12}O_{40}^{3-}$-IL, facilitated methyl orange degradation. Under optimal conditions, methyl orange degradation reached 95.98% and remained above 90% after five reuse cycles.

 doi:10.20944/preprints202511.1945.v1

The $C_8/PW_{12}O_{40}^{3-}$–IL Janus NPs offer a novel approach to the degradation of MO wastewater through a combination of targeted adsorption, efficient degradation, and practical separation. Their asymmetric architecture orchestrates a 'collect, degrade and leave' mechanism. The hydrophobic C_8 hemisphere acts as a molecular sponge, pre-concentrating methyl orange and drastically increasing its local availability to the adjacent catalytic hemisphere. There, the phosphotungstate-ionic liquid complex efficiently activates oxidants, generating hydroxyl radicals that rapidly cleave the azo chromophore and mineralise aromatic intermediates. The Janus morphology design, fortified by a magnetic Fe_3O_4 core, achieves exceptional degradation efficiency that rivals other catalysts. Crucially, it also solves the challenge of catalyst recovery, enabling instantaneous magnetic separation and robust reusability. This is a feature that eludes non-magnetic systems and outperforms simpler magnetic composites. This validates the strategic power of Janus organisation for creating intelligent, multifunctional materials that seamlessly integrate high catalytic activity with unparalleled practicality in the process for sustainable environmental technology.

Author Contributions: Material preparation, catalytic experiments and writing—original draft, Y.G.; writing—review & editing, D.X.; data analysis, X.Q., H.Y.; theoretical investigation, W.X.; original idea and supervision, J.D., S.H. All authors have read and agreed to the published version of the manuscript.

Funding: The study was supported by the university-level team research project of Hainan Vocational University of Science and Technology in 2024 "Research on Polyionic Liquid Materials and Their Catalytic Properties (HKKY2024-TD-17)"; Hainan Province 2025 Higher Education Teaching Reform Research Project: Research on the Ideological and Political Teaching Model of the "Principles of Chemical Engineering" Course Based on Target Problem-Oriented Approach (Hnjg2025ZC-127), Hainan Province 2025 Higher Education Scientific Research Project: Study on Polyionic Liquid Materials and Their Photocatalytic Performance (Hnky2025-66), Research on Teaching Methods of Mechanical Manufacturing Courses under Informationization Conditions (HKJG2024-35). The Hainan University of Science and Technology Vocational College Innovation and Entrepreneurship Training Program for College Students also provided support (2025).

Data Availability Statement: The data that support the findings of this study are available from the corresponding author upon reasonable request.

Conflicts of Interest: The authors declare no conflict of interest.

References

1. Gao, Hairong, et al. "Synthesis of Fe 3 O 4/GO magnetic nanomaterials and their adsorption of gentian violet dye." New Chemical Materials 51.11 (2023): 295-300.
2. Varjani S, Rakholiya P, Ng H Y, et al. Microbial degradation of dyes: an overview [J]. Bioresource Technology, 2020, 314: 123728.
3. Srivastava, Ankita, et al. "Emerging bioremediation technologies for the treatment of textile wastewater containing synthetic dyes: a comprehensive review." Journal of Chemical Technology & Biotechnology 97.1 (2022): 26-41.
4. Gao Y, Cao T, Du J, et al. The Bi-Modified (BiO) $2CO_3/TiO_2$ Heterojunction Enhances the Photocatalytic Degradation of Antibiotics[J]. Catalysts, 2025, 15(1): 56.
5. Richa, Choudhury A R. Synthesis of a novel gellan-pullulan nanogel and its application in adsorption of cationic dye from aqueous medium [J]. Carbohydrate polymers, 2020, 227: 115291.
6. Daniel-González, Guadalupe L., et al. "Characterization of the Enzymatic and Biosorption Processes Involved in the Decolorization of Remazol Brilliant Blue R Dye by Pleurotus ostreatus Pellets." Journal of Fungi 11.8 (2025): 572.
7. Cheng Y, Cao T, Xiao Z, et al. Photocatalytic treatment of methyl orange dye wastewater by porous floating ceramsite loaded with cuprous oxide [J]. Coatings, 2022, 12(2): 286.
8. Gao Y, Tieping Cao, et al. "Preparation of Bi@ Ho3+: TiO_2/Composite Fiber Photocatalytic Materials and Hydrogen Production via Visible Light Decomposition of Water." Catalysts 14.9 (2024): 588.
9. Yadav, Sonia, and Nadeem Sharma. "Cerium (III) phosphotungstate: an efficient catalyst in esterification of fatty acids." Zastita Materijala 65.4 (2024): 786-796.

 doi:10.20944/preprints202511.1945.v1

10. Sampurnam, S., et al. "A homogeneous Zr based polyoxometalate coupled with Ppy/PTA for efficient photocatalytic degradation of organic pollutants." Journal of Materials Science: Materials in Electronics 35.2 (2024): 122.
11. Maksimchuk, Nataliya V., et al. "Activation of H_2O_2 over Zr (IV). Insights from model studies on Zr-monosubstituted Lindqvist tungstates." ACS Catalysis 11.16 (2021): 10589-10603.
12. Kianfar, Ehsan. "Magnetic nanoparticles in targeted drug delivery: a review." Journal of Superconductivity and Novel Magnetism 34.7 (2021): 1709-1735.
13. Kyeong, San, et al. "Magnetic nanoparticles." Nanotechnology for Bioapplications. Singapore: Springer Singapore, 2021. 191-215.
14. Gao Y, Meng Q B, Wang B X, et al. Polyacrylonitrile Derived Robust and Flexible Poly (ionic liquid) s Nanofiber Membrane as Catalyst Supporter[J]. Catalysts, 2022, 12(3): 266.
15. Liu, Zhe, et al. "Janus particles: A review of their applications in food and medicine." Critical reviews in food science and nutrition 63.29 (2023): 10093-10104.
16. Chen et al. "Multi-stimuli-responsive polymer/inorganic janus composite nanoparticles." Langmuir 38.1 (2021): 422-429.
17. Galindo C, Jacques P, Kalt A. Photodegradation of the aminoazobenzene acid orange 52 by three advanced oxidation processes UV/H2O2, UV/TiO2 and VIS/TiO2 comparative mechanistic and kinetic investigations [J]. Journal of Photochemistry and Photobiology A: Chemistry, 2000, 130(1): 35-47.
18. Xue D, Meng Q B, Song X M. Magnetic-Responsive Janus nanosheets with catalytic properties [J]. ACS applied materials & interfaces, 2019, 11(11): 10967-10974.
19. Mahmoud, Maha M., Khaled Chawraba, and Soma A. El Mogy. "Nanocellulose: A comprehensive review of structure, pretreatment, extraction, and chemical modification." Polymer Reviews 64.4 (2024): 1414-1475.
20. Geßwein, Holger, et al. "A multipurpose laboratory diffractometer for operando powder X-ray diffraction investigations of energy materials." Applied Crystallography 55.3 (2022): 503-514.
21. Al-Harbi, Nuha, and Nabil K. Abd-Elrahman. "Physical methods for preparation of nanomaterials, their characterization and applications: a review." Journal of Umm Al-Qura University for Applied Sciences 11.2 (2025): 356-377.
22. Yan, Liu. "Precipitation behaviour of simulated high-level liquid waste during the denitration process based on two-step vitrification." Nuclear Engineering and Design 415 (2023): 112739.
23. Datye, Abhaya, and Andrew DeLaRiva. "Scanning electron microscopy (SEM)." Springer Handbook of Advanced Catalyst Characterization. Cham: Springer International Publishing, 2023. 359-380.
24. ** Yang, Qingze Chen, Jiaxin ** He, and Jianxi Zhu. "Nanoscale mineralogical characterization of terrestrial and extraterrestrial samples by transmission electron microscopy: A review." ACS Earth and Space Chemistry 7, no. 2 (2023): 289-302.
25. Nair, Gopika M., T. Sa**i, and Beena Mathew. "Advanced green approaches for metal and metal oxide nanoparticles synthesis and their environmental applications." Talanta Open 5 (2022): 100080.
26. Hao, X., Allgeyer, E. S., Lee, D. R., Antonello, J., Watters, K., Gerdes, J. A., ... & Bewersdorf, J. (2021). Three-dimensional adaptive optical nanoscopy for thick specimen imaging at sub-50-nm resolution. Nature methods, 18(6), 688-693.
27. Del Rosario, Mario, et al. "The field guide to 3D printing in optical microscopy for life sciences." Advanced Biology 6.4 (2022): 2100994.
28. Khalid, Khalisanni, Ruzaina Ishak, and Zaira Zaman Chowdhury. "UV–Vis spectroscopy in non-destructive testing." Non-destructive material characterization methods. Elsevier, 2024. 391-416.
29. Liu, Yucheng, et al. "Characterization of a novel cellulosic fiber from Broussonetia papyrifera L. bark for green-epoxy composite: Effect of fiber treatment." International Journal of Biological Macromolecules (2025): 144020.
30. Moronuki, Nobuyuki, Takeshi Takada, and Alexander Schotten. "Dynamic contact angle measurement on a microscopic area and application to wettability characterization of a single fiber." Langmuir 38.1 (2021): 72-78.

 doi:10.20944/preprints202511.1945.v1